Melting layer attenuation at Ka- and W-bands as derived from multi-frequency radar Doppler spectra observations

Haoran Li[1] and Dmitri Moisseev[1, 2]

[1] Institute for Atmospheric and Earth System Research / Physics, Faculty of Science, University of Helsinki, Finland

[2] Finnish Meteorological Institute, Helsinki, Finland.

Corresponding author: Haoran Li (haoran.li@helsinki.fi)

Key Points:

- Ka-/W-band melting layer attenuation is derived
- The melting layer attenuation is derived by analyzing X-, Ka- and W-band radar Doppler spectra
- Presented results are in good agreement with previously reported melting layer modeling results for rain rates smaller than 3 mm/h

Abstract

The melting layer of precipitation has a major impact on remote sensing and telecommunications. However, there is a shortage of observational studies to validate and constrain the melting layer models especially for high-frequency radar bands. In this paper, we report how multi-frequency radar Doppler spectra can be used to retrieve the melting layer attenuation at Ka- and W-bands. The presented analysis is based on identifying Rayleigh scattering regions in radar Doppler spectra measurements where dual-wavelength spectral ratios can be related to differential attenuation. We show that the estimated attenuation at Ka- and W-bands agrees reasonably well with previously reported studies, but there are indications of differences at higher rain rates. We advocate that this technique can be applied to long-term observations to advance our knowledge of the melting process. The parameterizations of melting layer attenuation as a function of rain rate and radar reflectivity are also presented.

Plain Language Summary

While the melting layer is a relatively narrow layer in precipitation systems, it has a significant impact on telecommunication and remote sensing applications. For spaceborne and ground-based radar measurements, unaccounted attenuation in the melting layer may cause significant errors in retrievals of rainfall rate and ice cloud properties, respectively. There are two approaches to quantify attenuation in the melting layer, namely through modeling or observations. Modeling studies have been carried out and are reported in the scientific literature, however, it is acknowledged that there is a shortage of observational studies that could help us to constrain the models. In this paper, we present a study that utilizes radar Doppler spectra recorded at X-, Ka- and W-bands to retrieve melting layer attenuation. We show that the estimated attenuation at Ka-

23 and W-bands agrees reasonably well with previous studies, but there are indications of
24 differences at higher rain rates. With the utilization of this technique, long-term observations are
25 expected to advance our knowledge of the melting process, as well as modeling of the melting
26 layer attenuation for applications in millimeter-wavelength radars, passive microwave remote
27 sensing, 5G/6G commercial links and space-Earth telecommunications.

28 **1 Introduction**

29 The melting layer of precipitation is an area where snowflakes melt into raindrops. In this layer
30 the hydrometeors undergo rather complex microphysical processes, while changing from
31 irregularly-shaped ice particles into spheroid-like water drops [Matsuo & Sasyo, 1981;
32 Yokoyama & Tanaka 1984; Fabry & Zawadzki, 1995; Leinonen & von Lerber, 2018]. In
33 traditional weather radar observations, the melting layer can be identified by the enhanced radar
34 reflectivity factor, the so-called “bright band”, which is caused among other things by the change
35 in the hydrometeor dielectric properties. Propagation of radio waves through the melting layer
36 could lead to a detectable attenuation which is comparable to the path-integrated rain attenuation
37 [Bellon et al., 1997; Kollias & Albrecht, 2005]. Although melting layer attenuation does not pose
38 major problems for cm-wavelength radars if the propagation path through the layer is not too
39 long [von Lerber et al. 2015], it is considerable at mm wavelengths and affects the interpretation
40 of ground- and space-based cloud and precipitation radar observations [Illingworth et al., 2007;
41 Mitrescu et al., 2010]. For passive satellite microwave remote sensing, the absence of an accurate
42 estimate of excess extinction in the melting layer may also lead to significant errors [Bauer et al.,
43 1999; Battaglia et al., 2003]. In addition, quantifying melting layer attenuation at millimeter
44 wavelengths becomes increasingly important as the radio waves in commercial communications

[Siles et al., 2015] and Earth-satellite links [Panagopoulos et al., 2004] move towards higher frequency bands.

There are two main approaches for estimating the radar signal attenuation in the melting layer, namely model- or observation-based. In the literature, there are a number of modeling studies that somewhat differ in the parametrizations used in the microphysical and/or electromagnetic parts of the models [e.g., Zhang et al., 1994; Russchenberg & Ligthart, 1996; D'Amico et al., 1998; Fabry & Szyrmer, 1999; Olson et al., 2001; Skaropoulos & Russchenberg, 2003; Matrosov, 2008; Liao et al., 2009; Planche et al., 2014; von Lerber et al. 2015]. Most of these models are capable of reproducing observed profiles of radar reflectivity factor [Russchenberg & Ligthart, 1996; D'Amico et al., 1998; Fabry & Szyrmer, 1999; Matrosov, 2008; Liao et al., 2009; von Lerber et al. 2015], dual-polarized variables [Russchenberg & Ligthart, 1996] or Doppler velocity profiles [Fabry & Szyrmer, 1999; Skaropoulos & Russchenberg, 2003]. Using such a modeling approach, attenuation caused by the melting layer can be estimated [e.g., von Lerber et al., 2015]. At mm wavelengths, melting layer models are capable of reproducing radar signatures, such as the distinct “dark band” at the upper part of the melting layer [Kollias & Albrecht, 2005]. However, due to the lack of knowledge on thermodynamical [Leinonen & von Lerber, 2018] and scattering processes [Botta et al., 2010; Johnson et al., 2016] that take place during melting, the computed melting layer attenuation values are expected to be uncertain. For example, two widely used studies [Matrosov, 2008; Haynes et al., 2009] differ in the computed W-band attenuation values. Therefore, it is important to validate such estimates by measurements.

Previously, such measurements were carried out by using cm-wavelength radars. Bellon et al. [1997] have used coinciding X-band and UHF profiling radar observations to retrieve melting layer attenuation at X-band. Since precipitation observations at both frequency bands fall within

68 the Rayleigh regime, the observed reflectivity value difference can be linked to the attenuation.
69 Due to the presence of non-Rayleigh scattering and potential additional attenuation (e.g., from
70 supercooled liquid water) this approach is not directly applicable at higher frequencies.
71 Nakamura et al. [2018] have proposed to use two Ka-band radars located on a mountain slope to
72 estimate melting layer attenuation at this frequency. The setup is difficult to replicate and there
73 appears to be a lack of direct measurements of melting layer attenuation at mm wavelengths,
74 especially at W-band. This study aims to address this topic.

75 Since several years, multi-frequency Doppler spectra observations are being recorded at a
76 number of measurement sites. This research uses multi-frequency Doppler spectra observations
77 collected by the US DOE Atmospheric Radiation Measurement (ARM) 2nd mobile facility
78 (AMF2) during the Biogenic Aerosols Effects on Clouds and Climate (BAECC) field campaign
79 in Finland [Petäjä et al., 2016]. At vertical incidence, radar Doppler spectra separate radar signals
80 from hydrometeors according to their fall velocities [e.g., Kollias et al., 2002; Moisseev et al.,
81 2006; Spek et al., 2008]. Since smaller particles usually fall slower, there may be a part of the
82 Doppler spectrum where the scattering from observed hydrometeors can be described using the
83 Rayleigh approximation even at W-band [Tridon et al., 2013; Kneifel et al., 2016].

84 In this paper, we demonstrate the use of this “Rayleigh region” in multi-frequency radar Doppler
85 spectra to derive melting layer attenuation. The proposed method can be used to correct for this
86 attenuation in multi-frequency Doppler radar measurements. However, as discussed later in the
87 article, matching the radar volumes is very important for the optimal performance of the method.
88 That is why our focus is on deriving the parametrizations and validating results of previously
89 reported melting layer attenuation studies, using carefully selected observations.

The topic presented in this work is of direct relevance to the cloud and precipitation remote sensing communities working with ground- and space-based observations. Furthermore, the study supports current and future cloud and precipitation satellite missions, namely the National Aeronautics and Space Administration (NASA) CloudSat, Global Precipitation Measurement mission (GPM), and the European Space Agency/Japan Aerospace Exploration Agency (ESA/JAXA) Earth Clouds, Aerosols and Radiation Explorer (EarthCARE).

This paper is organized as follows. Section 2 presents the measurement setup and associated data processing. Then, section 3 describes the procedure of this new technique and discusses the retrieval uncertainties. A "sanity" check, a case analysis as well as the retrieved melting layer attenuation are presented in section 4 and conclusions are summarized in section 5.

2 Measurements

The rain events analyzed in this study were collected during the BAECC field campaign, which was carried out at the University of Helsinki Hyytiälä Station from February to September 2014 [Petäjä et al., 2016]. The radar data were recorded by the X/Ka-band scanning Atmospheric Radiation Measurement (ARM) cloud radar (X/Ka-SACR) as well as by the zenith-pointing Ka-band (KAZR) and W-band ARM cloud radars (MWACR) [Kollias et al., 2014; Kneifel et al., 2015; Falconi et al., 2018]. X- and Ka-SACR are dual-polarization radar systems that record the copolar correlation coefficient and the linear depolarization ratio, respectively. The range gate spacing for X/Ka-SACR and KAZR is 25 m, 5 m less than that of MWACR. All the radars were recording Doppler spectra every 2s using 512-sample Fast Fourier Transform (FFT) that resulted in the velocity resolution of about 2.3 cm/s for all the radars. The original spectra were averaged and the resulting temporal resolution is 14 s. The half-power beam widths of the X-SACR, Ka-SACR, KAZR and MWACR radars are 1.27°, 0.33°, 0.33° and 0.38° respectively.

The data used in this study were collected when all the radars were pointing vertically. To maximize the matching between measurements at various frequencies, X/Ka-SACR measurements were used for analysis of X/Ka-band spectra, while KAZR and MWACR data were used for the Ka/W-band spectra. The retrieval of W-band attenuation was done based on KAZR/MWACR combination, in which Ka-band attenuation was derived from Ka-SACR and X-SACR observations. This is done because the horizontal distance between X-SACR and MWACR was about 17 m [Petäjä et al., 2016], while the distance between KAZR and MWACR was just a couple of meters.

It should be noted that MWACR had a small antenna pointing error of about 0.5 to 1°, caused by freezing and thawing of the gravel under the radar container, which has led to some offset in measured vertical Doppler velocity [Kneifel et al., 2016]. Furthermore, due to the difference in the radar volumes, it was observed that in some cases X- and Ka- band spectra were not well matched. To minimize the associated errors, the MWACR (X-SACR) spectra were shifted until the best match with the KAZR (Ka-SACR) measured spectra was reached [Kneifel et al., 2016]. It was found, however, that in the ice region the matching of single-peak spectra was very difficult to achieve. Given that there is no reliable indicator (e.g., presence of detectable small peaks or valleys) for identifying a good spectra match, the resulting uncertainty in dual-wavelength spectral ratios can be as large as the expected attenuation contribution. For multi-peak spectra this uncertainty can be mitigated. Because of this, in this study only cases with multi-modal spectra in the snow region were used. Additionally, the size of the Rayleigh region in W-band Doppler spectra can be rather small and is easily affected by turbulent broadening [Tridon & Battaglia, 2015]. The broadening of spectra due to turbulence and cross-wind [Doviak & Zrnic, 1984] results in power leakage from non-Rayleigh scattering spectra regions into the

Rayleigh region and therefore biases the needed DSR measurements. That is why Ka/W-band spectra analyses were only performed on cases with a well-defined supercooled water peak [Luke et al., 2010].

Prior to analyzing the radar data, gaseous attenuation was corrected by applying the millimeter-wave propagation model [Liebe, 1985] which was computed using the closest radio sounding data, which were carried out four times per day [Petäjä et al., 2016].

To verify X-SACR calibration and to compute rain specific attenuation at all the frequencies, radar variables were computed from 2D video distrometer [Schuur et al., 2001] observations by using Python implementation of T-matrix scattering calculations (PyTmatrix) [Mishchenko & Travis, 1994; Wielaard et al., 1997; Leinonen, 2014]. The melting layer attenuation method is based on “dual-wavelength spectral ratio” measurements, as discussed in the next section, and therefore is independent of potential reflectivity calibration offsets. That is why no calibration is needed for Ka-SACR, KAZR or MWACR. The X-SACR reflectivity values, however, are used to derive parametrizations of melting layer attenuation as a function of radar reflectivity and rain rate, which are affected by the calibration bias as well as the radome attenuation. To mitigate this, the X-SACR calibration was done by matching the observed reflectivity at about 500 m to the reflectivity values computed from the 2D video disdrometer data. The time lag between the observed and simulated radar reflectivity values was found to be around 1 min. Note that we did not use the lowest range gate of X-SACR due to the near-field effects [Sekelsky, 2002; Falconi et al., 2018].

3 Methods

3.1 General description

Generally, radar signal attenuation through clouds and rain is greater at higher frequencies, resulting in so-called differential attenuation between radio waves of collocated radars operating at distinct frequencies [Tuttle & Rinehart, 1983]. If the radars observe weather echoes where hydrometeors are small enough to fall within the Rayleigh regime, the ratio of the observed reflectivity factors, the dual-wavelength ratio (DWR), is mainly caused by the differential attenuation. This measurement has been used to retrieve the liquid water content from dual-wavelength radar observations, since most liquid droplets are good Rayleigh scatterers at Ka-band [Ellis & Vivekanandan, 2011] as well as at W-band [Hogan et al., 2005]. By applying the DWR method to vertically pointing X-band and UHF profiling radars measurements, Bellon et al. [1997] have estimated the melting layer attenuation at X-band, as the sizes of most hydrometeors below and above the melting layer are much smaller than the X-band wavelength.

However, the DWR method cannot be directly applied to retrieve the attenuation when the hydrometeors are not Rayleigh scatterers [Gaussiat et al., 2003]. Tridon et al. [2013] have proposed to use the slower falling part of the vertically pointing Doppler spectra, where the Rayleigh assumption is valid, to study the attenuation in rainfall.

Similar to rainfall, in the ice part of the precipitation the slower falling particles should be small enough to be Rayleigh scatterers. Spek et al. [2008] have reported that spectral dual-polarization radar signatures of these particles are similar to those of ice crystals. Kneifel et al. [2016] have shown that spectral multi-frequency observations in this Doppler spectrum part behave in accordance with the Rayleigh scattering approximation.

178 Figure 1 demonstrates multi-frequency Doppler spectra properties above and below the melting
179 layer as was discussed above. As shown in Figure 1 (a), the melting layer can be recognized by
180 the enhanced radar reflectivity. The melting layer boundaries, shown in the figure and used in
181 this study, were estimated using X-SACR measurements of the copolar correlation coefficient
182 [Ryzhkov & Zrnic, 1998; Matrosov et al., 2007]. The derivation of the differential attenuation in
183 Figure 1 (a) is highly dependent on the identification of the Rayleigh region, as illustrated in
184 panels (b) to (e), and will be discussed in the next section.

185 Assuming that multi-frequency Doppler radar spectra are well-matched, the Rayleigh parts of the
186 spectra can be recognized by the plateau in the observed spectral dual-wavelength spectral ratios
187 (DSR). The observed DSR values in the Rayleigh part of the Doppler spectra above the melting
188 layer will be caused by differential attenuation due to combined wet radome, rain, and melting
189 layer, as well as possible calibration offsets. The same factors, except for the melting layer
190 attenuation, contribute to DSR values in the Rayleigh region in rain. Therefore, by considering
191 the differences of the dielectric factors for hydrometeors below and above melting layer, the
192 differential melting layer attenuation can be estimated as:

$$A_{\mathrm{ML}}(\lambda_1,\lambda_2) = \overline{DSR_{\mathrm{Rayleigh,\ above\ ML}}(\lambda_1,\lambda_2)} - \overline{DSR_{\mathrm{Rayleigh,\ below\ ML}}(\lambda_1,\lambda_2)} - 10\log_{10}\left(\frac{\left|K_{\mathrm{above\ ML}}(\lambda_1)\right|^2\left|K_{\mathrm{below\ ML}}(\lambda_2)\right|^2}{\left|K_{\mathrm{below\ ML}}(\lambda_1)\right|^2\left|K_{\mathrm{above\ ML}}(\lambda_2)\right|^2}\right),\ [\mathrm{dB}] \quad (1)$$

193 where λ_1 and λ_2 are 30.9 mm and 8.5 mm (X- and Ka-SACR) or 8.6 mm and 3.19 mm (KAZR
194 and MWACR) respectively. $\left|K_{\mathrm{above\ ML}}(\lambda)\right|^2$ is the dielectric constant of ice (X/Ka) or supercooled
195 water droplets (Ka/W) at λ and $\left|K_{\mathrm{below\ ML}}(\lambda)\right|^2$ is the dielectric constant of rain water at λ.
196 $\overline{DSR_{\mathrm{Rayleigh,\ above\ ML}}(\lambda_1,\lambda_2)}$ stands for the average DSR in the Rayleigh part of the spectrum just

197 above the melting layer (ice for X/Ka, liquid water for Ka/W), $\overline{DSR_{\text{Rayleigh, below ML}}(\lambda_1,\lambda_2)}$ is the
198 same but for below the melting layer (rain). As can be seen in Figure 1 (b, c), the supercooled
199 water DSR values are higher than those of ice. This difference can be explained by the fact that
200 the dielectric constants of ice at W-, Ka- and X-bands are almost the same, while the dielectric
201 constants of liquid water at these radar frequencies are different. Here $\overline{DSR_{\text{Rayleigh}}(\lambda_1,\lambda_2)}$ is
202 defined as

$$\overline{DSR_{\text{Rayleigh}}(\lambda_1,\lambda_2)} = 10\log_{10}\left(\frac{\sum_{v_i=v_{\text{start}}}^{v_{\text{end}}} S_{\lambda_1}(v_i)}{\sum_{v_i=v_{\text{start}}}^{v_{\text{end}}} S_{\lambda_2}(v_i)}\right), \text{[dB]} \quad (2)$$

203 where v_{start} and v_{end} are velocity boundaries of Rayleigh region and will be discussed later;
204 $S_{\lambda_1}(v)$ and $S_{\lambda_2}(v)$ are spectral powers in linear scale at v observed by radars working at λ_1 and
205 λ_2 respectively. As can be seen in Figure 1(a), the differential attenuation for Ka/W is about 3
206 times of that for X/Ka in rain. Their difference at 500 m is mainly due to the radome attenuation,
207 rain attenuation and other calibration issues. There is no significant increase of the differential
208 attenuation for either X/Ka or Ka/W in snow. The differential attenuation in the melting layer is
209 larger for Ka/W than for X/Ka, confirming that the W-band signal is attenuated more than the
210 Ka-band upon propagation through the melting layer.

211 The above-described procedure provides melting layer differential attenuation values for X/Ka
212 and Ka/W band radar observations. To retrieve absolute attenuation values, we use modeling
213 results of Matrosov [2008] that links melting layer attenuation to rain intensity for X-band radar
214 observations.

3.2 Identification of Rayleigh scatterers in Doppler spectra

The most important and somewhat challenging part of the presented method is the identification of the Rayleigh scatterers in the observed radar Doppler spectra. In this study we have used three distinct approaches for this, depending on the considered frequency bands and whether we are dealing with measurements in rain or snow.

For all frequency bands in rain we follow the approach of Tridon et al. [2013], who have demonstrated that the DSR in rain exhibit a well-defined plateau in the low-velocity region, which is defined by small raindrops that satisfy the Rayleigh scattering assumption. Analysis of the cases used in this study shows that the DSR plateau extends up to velocities of 2.5 ~ 3.5 m/s and 4 ~ 5 m/s for Ka/W and X/Ka spectral ratios, respectively, see Figure 1 (d, e) for an example. Tridon & Battaglia [2015] have shown that the spectral broadening, due to air motion, could affect the Rayleigh plateau and bias the DSR measurements. To mitigate this, the optimal estimation method has been utilized [Tridon & Battaglia, 2015; Tridon et al., 2017a; Tridon et al., 2017b]. After inspecting the cases analyzed in this paper (see the list in the supporting information), we found that the DSR in the Rayleigh region is rather flat and does not seem to be affected by the spectral broadening, which would skew the plateau [Tridon et al., 2013]. This applies to X/Ka and Ka/W DSR observations. Furthermore, in the majority of cases the Ka/W DSR exhibit distinct resonance scattering peaks in the larger raindrop region, see Figure 1 (e), which is also an indication of low turbulence conditions [Tridon et al., 2013]. Therefore, it is expected that the derived combined attenuation due to wet radome and rain, as well as possible calibration offsets can be estimated from the DSR Rayleigh plateaux in rain. To minimize the impact of noise, the summation limits in (2) were determined as follows: v_{start} is defined as Doppler velocity where the signal-to-noise ratio (SNR) reaches 10 dB and the width of the

Rayleigh plateau, v_{end} - $v_{start,}$ is estimated to be 2 m/s and 1.5 m/s for X/Ka and Ka/W, respectively.

The identification of Rayleigh scatterers above the melting layer is more involved and depends on the frequency band. Because ice particle velocities do not change as much with size as velocities of raindrops, the Rayleigh plateau region is smaller in snow than in rain, as can be seen in Figure 1 (b, c). Analysis of our data shows that X/Ka DSR Rayleigh plateau extends over at least 0.5 m/s. Therefore, for X/Ka in snow, an SNR of 10 dB was adopted to determine v_{start} and the value of v_{end} depends on the extent of Rayleigh plateau. To avoid the potential impact of turbulence, cases with slanted Rayleigh region, namely not a flat plateau, due to significant spectral broadening were removed.

Locating the Rayleigh region in snow for W-band seems to be more difficult due to its relatively narrow span. However, liquid water droplets in cloud are small enough to satisfy Rayleigh scattering assumptions at Ka- and W- bands [e.g., Gaussiat et al., 2003; Hogan et al., 2005]. In radar Doppler spectra, the supercooled liquid water can be identified as a narrow well-defined peak close to zero Doppler velocity [Zawadzki et al., 2001; Luke et al., 2010; Shupe et al., 2004]. That is why we have used supercooled water peak, visible and distinct in Figure 1 (c) just above the melting layer, for computing DSR and estimating the differential attenuation between Ka-band and W-band. Another benefit of adopting the supercooled water is that the total spectral power of this peak is almost not affected by turbulence. Observations show that such supercooled water peaks barely exceed the noise level by a few dBs, thus lower SNR (3 dB) was adopted to determine v_{start} and v_{end}. By contrast, the Rayleigh plateau in ice is used for X/Ka-band observations since the supercooled water peaks detected by Ka- and W-band radars are not always detectable by X-SACR.

3.3 Uncertainty analysis

There are two uncertainty types relevant to this study, namely statistical and methodological. The estimation of the differential attenuation includes computations of DSR below and above melting layer. Ignoring the much smaller contribution from the dielectric factor term in (1), the statistical uncertainty of Ka-band melting layer attenuation is defined as

$$\Delta A_{\mathrm{ML,Ka}} = \sqrt{\Delta\overline{DSR}_{\mathrm{Rayleigh,\ above\ ML}}(X,Ka)^2 + \Delta\overline{DSR}_{\mathrm{Rayleigh,\ below\ ML}}(X,Ka)^2} \tag{3}$$

Following the method utilized by Hogan et al. [2005], $\Delta\overline{DSR}_{\mathrm{Rayleigh}}(X,Ka)$ for high SNR may be expressed as

$$\Delta\overline{DSR}_{\mathrm{Rayleigh}}(X,Ka) = \sqrt{\left(\frac{4.343\sqrt{\sum_{v_i=v_{\mathrm{start}}}^{v_{\mathrm{end}}}\left(\frac{S_{\mathrm{X}}(v_i)}{\sqrt{M}}\right)^2}}{\sum_{v_i=v_{\mathrm{start}}}^{v_{\mathrm{end}}} S_{\mathrm{X}}(v_i)}\right)^2 + \left(\frac{4.343\sqrt{\sum_{v_i=v_{\mathrm{start}}}^{v_{\mathrm{end}}}\left(\frac{S_{\mathrm{Ka}}(v_i)}{\sqrt{M}}\right)^2}}{\sum_{v_i=v_{\mathrm{start}}}^{v_{\mathrm{end}}} S_{\mathrm{Ka}}(v_i)}\right)^2}, \text{[dB]} \tag{4}$$

$$= \frac{4.343}{\sqrt{M}}\sqrt{\frac{\sum_{v_i=v_{\mathrm{start}}}^{v_{\mathrm{end}}} S_{\mathrm{X}}(v_i)^2}{\left(\sum_{v_i=v_{\mathrm{start}}}^{v_{\mathrm{end}}} S_{\mathrm{X}}(v_i)\right)^2} + \frac{\sum_{v_i=v_{\mathrm{start}}}^{v_{\mathrm{end}}} S_{\mathrm{Ka}}(v_i)^2}{\left(\sum_{v_i=v_{\mathrm{start}}}^{v_{\mathrm{end}}} S_{\mathrm{Ka}}(v_i)\right)^2}}$$

where M is the number of independent samples. The numbers of sample averaged in raw data products are 3, 11 and 5 for X-SACR, Ka-SACR/KAZR and MWACR respectively. In this study, we have used averaging over seven continuous Doppler spectra products, implying M = 21 (X-SACR), 77 (Ka-SACR/KAZR) and 35(MWACR).

For W-band attenuation the uncertainty can be expressed as

$$\Delta A_{\mathrm{ML,W}} = \sqrt{\Delta A_{\mathrm{ML,Ka}}{}^2 + \Delta\overline{DSR_{\mathrm{Rayleigh,\ above\ ML}}(Ka,W)}^2 + \Delta\overline{DSR_{\mathrm{Rayleigh,\ below\ ML}}(Ka,W)}^2} \quad (5)$$

We found that $\Delta A_{\mathrm{ML,Ka}}$ and $\Delta A_{\mathrm{ML,W}}$ of our estimates are 0.4 ~ 0.6 dB and 0.55 ~ 0.75 dB respectively, mainly depending on the number of spectra averaged.

The methodological uncertainties include potential errors caused by imperfectly-matched Doppler spectra at various wavelengths and computations of the absolute values of melting layer attenuation from the differential attenuation. To derive the absolute values of the melting layer attenuation, the relations linking X-band melting layer attenuation to rain rate proposed by Matrosov [2008] are used. Von Lerber et al. [2015] have shown that the melting layer attenuation depends on ice particle properties, i.e. whether they are rimed or unrimed. In the cases we have collected, the maximum reflectivity (from X-SACR) at melting layer peak is about 41 dB, which may correspond to around 1 dB X-band attenuation according to [Bellon et al., 1997]. The corresponding value estimated by Matrosov [2008] is about 0.26 dB. Therefore, Matrosov's relations could underestimate or overestimate the attenuation. In this study, most melting layer cases are associated with rimed snowflakes as revealed by the supercooled water peaks, thus we expect that the X-band attenuation should be on the smaller side according to [von Lerber et al. 2015]. Assuming that the actual X-band attenuation is 0.2 to 5 times that of Matrosov's relation, the expected error of the melting layer attenuation at X-band ranges from -1.04 (underestimation) to 0.21 (overestimation) dB. This translates to 20 ~ 30% error at Ka-band and < 10% at W-band in dB scale.

The uncertainties associated with Doppler spectra matching are difficult to quantify. In rain, the expected large Rayleigh plateau facilitates the matching. In snow, we have used multi-mode spectra for matching.

4 Results

From all the rain cases recorded during BAECC, seven stratiform rain events were selected to estimate the Ka-band melting layer attenuation (~ 48 min in total). These cases have satisfied our criteria, namely presence of multimodal spectra in ice region. From these cases, only three events showed detectable supercooled liquid water peaks (~ 24 min in total) and were used to compute W-band attenuation (see supporting material for the list).

4.1 "Sanity" check, comparison against cloud top DWR

To verify whether our retrieval is meaningful, a comparison was made to the DWR at the cloud top (DWR_{CT}) where the Rayleigh assumption is valid. Therefore, the retrievals based on the DWR_{CT} and the DSR at melting layer top (DSR_{ML_top}) would be the same if there were no attenuation between the melting layer top and cloud top. However, the fact is that such attenuation due to snow and supercooled water above the melting layer could be significant, especially at W-band [Kneifel et al., 2015]. Therefore, we expect that the results of the presented technique (DSR_{ML_top}) should always be smaller than the estimates using the DWR_{CT}-based method.

To derive DWR_{CT}, the area of cloud top where Rayleigh's assumption applies needs to be identified. Hogan et al. [2000] have observed that the radar reflectivity of Rayleigh scatterers in ice clouds at W-band is below -20 dBZ, but it seems that the threshold of -15 dBZ or higher can also be used [Stein et al., 2015]. After analysing the DWR_{CT} profiles, we found that the snow with reflectivity between -20 and -10 dBZ observed by X-SACR may also be treated as Rayleigh scatterers at W-band. The radar reflectivity where the Rayleigh assumption is satisfied seems to be dependent on snow type, which, however, is not the topic of this paper. In addition, the DWR_{CT} values are not stable when SNR is low, since the radar signal at the highest detected

317 cloud top is affected by noise. In this comparison, the cloud top where X-band radar reflectivity
318 ranges from -20 dBZ to -10 dBZ and all radars' SNR > 10 dB was used to calculate DWR_{CT}.

319 In Figure 2 the results of this comparison are shown. Note that the radome and rain attenuation
320 was removed from DWR_{CT} and DSR_{ML_top} values by subtracting DSR in the Rayleigh plateau
321 derived just below the melting layer. As expected, the DWR_{CT}-based retrievals are larger than
322 DSR_{ML_top}-based for X/Ka as well as for Ka/W, indicating the non-negligible attenuation above
323 the melting layer top. Furthermore, the difference between the two approaches is larger for Ka/W
324 than for X/Ka -bands. More specifically, the difference between the results from DWR_{CT} and
325 DSR_{ML_top} can be as large as 1.5 dB for X/Ka and 4 dB for Ka/W in 11th May 2014, an event
326 with significant supercooled water signatures in spectra observations. While this figure does not
327 prove that the derived melting layer attenuation values are correct, it gives a level of confidence
328 that our retrievals are reasonable.

329 **4.2 Case study, May 11th 2014**

330 On May 11th 2014, a stratiform precipitation system passed over the Hyytiälä station. During
331 BAECC the X-SACR and Ka-SACR were regularly performing range height indicator (RHI)
332 scans and the Doppler spectra data are not continuous. Only a short period of about 22 min when
333 all radars were pointing vertically is available for this event.

334 In Figure 3 (a), the X-SACR height time observations of reflectivity factor are shown. As can be
335 seen the bright band is clearly visible and its height is around 1.2 km. There are three short
336 periods of rain showers around 03:05, 03:15 and 03:20 UTC. The precipitation cloud top height
337 is about 3 km. There is also a second cloud layer, which starts just below 4 km. The upper cloud
338 is an ice cloud and particles in its upper part can be regarded as Rayleigh scatterers.

To compute the differential attenuation, both DSR and DWR observations were corrected for rain, radome attenuations and calibration offsets by subtracting estimated just below the melting layer. That is why DWR(X, Ka) values become negative in rain. This effect for DWR(Ka, W) is obscured by the non-Rayleigh scattering. The influence of differential attenuation on observations is clearly visible in the DWR measurements of the upper cloud, Figure 3 (b, d).

The comparison of the differential attenuation estimates using DSR_{ML_top} and DWR_{CT} are shown in Figure 3 (c, e). As expected DWR_{CT}-based estimates are higher, because they also include attenuation due to snow and possibly supercooled liquid water. The melting layer differential attenuation between X-band and Ka-band (Figure 3c) shows dependence on precipitation intensity, namely the higher the precipitation intensity, the larger the melting layer attenuation. Such dependence can also be found in Figure 3 (e), however, with smaller relative variations.

The biggest difference between DWR_{CT} and DSR_{ML_top} observations is found around 03:10 UTC and can be seen in Figure 3 (e). This larger difference between the DWR_{CT} and DSR_{ML_top} values is most probably due to the attenuation above the melting layer, which is possibly caused by supercooled water that attenuates more at W-band.

Overall the comparison of DWR_{CT} and DSR_{ML_top} based differential attenuation retrievals show that DWR_{CT} tends to overestimate the melting layer attenuation. Even though the attenuation due to snow could potentially be accounted for (e.g. Leinonen et al., [2011]), the attenuation from supercooled liquid water cannot be currently removed.

4.3 Parametrizations of melting layer attenuation

It is customary to express the melting layer attenuation either as a function of precipitation rate or unattenuated reflectivity below the melting layer. For this we have used disdrometer corrected X-band reflectivity values and rain rates derived from these values. We have decided not to use

362 the surface rain rate measured by one of our ground-based precipitation sensors, because of the
363 potential rain evaporation [Tridon et al., 2017b]. The disdrometer-corrected X-band reflectivity
364 beneath the melting layer was converted to rain rates by the Z-R relations, which were derived
365 from the hourly disdrometer data and not from the whole events (see the comparison in
366 supporting material). This approach allows for adaptive Z-R conversions. It should be noted, that
367 in order to compute the W-band attenuation, not only the differential attenuation between Ka-
368 band and W-band but also the X-/Ka-band differential attenuation should be derived. Since the
369 selection criteria for Ka/W and X/Ka spectra analysis cases are not the same, not in all cases
370 Ka/W and X/Ka differential attenuation values can be estimated simultaneously. In such
371 situations, the closest retrieved Ka-band attenuation value, within 1-min of Ka/W spectra
372 observations, was used as the input in calculating the W-band attenuation.

373 In addition to total attenuation, specific melting layer attenuation was also computed. The
374 specific attenuation is defined as the total attenuation divided by the melting layer thickness.
375 Additionally, the rain specific attenuation values, for the studied cases, were computed from the
376 disdrometer data by using PyTmatrix.

377 In Figure 4, the derived parametrizations are presented and compared to the attenuation-rain rate
378 (A-R) expressions of Matrosov, [2008]. In Figures 4 (a_1, b_1), the rain rate in Matrosov [2008]
379 relations was converted to the radar reflectivity factor by applying the Marshall and Palmer
380 relation, i.e. $Z = 200R^{1.6}$ [Marshall and Palmer 1948; Marshall et al., 1955]. As can be seen, the
381 melting layer attenuation for Ka- and W-bands depends on the reflectivity factor, rain rate, as
382 well as the melting layer thickness. The melting layer thickness increases as the reflectivity
383 factor rises, which is in agreement with previous studies [e.g., Fabry & Zawadzki, 1995;
384 Wolfensberger et al., 2016]. Similar to Bellon et al. [1997], we found that the melting layer peak

reflectivity at X-band seems to be better correlated to melting layer attenuation than the rain rate (see supporting material).

As shown in Figure 4 (a, b), the observed results both for Ka- and W- bands agree reasonably well with Matrosov's relations, at least in cases where the rain rate is less than 3 mm/h ($Z < 30$ dBZ). Such good agreement is noteworthy, given the recent discussion of the applicability of the Effective-Medium Approximation (EMA) for modeling scattering properties of snowflakes and melting ice particles [Johnson et al., 2016]. It could possibly be explained by the fact that the forward scattering computations do not necessarily need complex particle models, as shown by scattering computations of snowflakes [e.g., Tyynelä et al., 2013, Hogan and Westbrook, 2014; Hogan et al., 2017; Leinonen et al., 2018]. However, these studies focused on dry snowflakes and no similar computations for melting particles were done.

For higher rain rates ($Z > 30$ dBZ), the observations show smaller attenuation values than the model despite the fact that a very limited number of cases were analyzed. It is interesting to note that this difference between the model and observations is similar for Ka- and W-bands. This attenuation overestimation in modeling results might be due to the assumptions made about snow physical properties. The model assumes that the snowflakes are unrimed/lightly rimed [Matrosov, 2008], whilst most of our observation cases, especially when $Z > 30$ dBZ, exhibit well-defined supercooled water signatures which could lead to higher degrees of riming. Von Lerber et al. [2015] have shown that under similar conditions, i.e. rain intensity, the rimed snowflakes would lead to lower melting layer attenuation. It should also be noted that, in addition to density, snowflake shape is also affected by riming [Li et al., 2018], which may have a significant impact on scattering properties of ice particles especially at mm wavelengths.

The fitted relations for melting layer attenuation (dB) at Ka-band are

$$A_{Ka} = 0.97R^{0.61} \text{ or } A_{Ka} = 0.13Z_{\text{lin}}{}^{0.38} \text{ (Z}_{\text{lin}} \text{ is reflectivity in mm}^6/\text{m}^3\text{)}, \quad (6)$$

and at W-band,

$$A_W = 2.9R^{0.42} \text{ or } A_W = 0.67Z_{\text{lin}}{}^{0.27} . \quad (7)$$

As shown in Figure 4 (c) and (d), the melting layer specific attenuation at Ka- and W-bands increases with reflectivity factor and rain rate as well as melting layer width. Compared to rain, the specific attenuation in the melting layer is significantly larger. The derived relations for melting layer and rain one-way specific attenuations at Ka-band are as follows,

$$k_{ML\_Ka} = 1.2R^{0.42} \text{ or } k_{ML\_Ka} = 0.29Z_{\text{lin}}{}^{0.27}, \quad (8)$$

$$k_{rain\_Ka} = 0.18R^{1.24} \text{ or } k_{rain\_Ka} = 0.0074Z_{\text{lin}}{}^{0.67}, \quad (9)$$

and at W-band,

$$k_{ML\_W} = 3.4R^{0.3} \text{ or } k_{ML\_W} = 1.2Z_{\text{lin}}{}^{0.2}, \quad (10)$$

$$k_{rain\_W} = 1.12R^{0.93} \text{ or } k_{rain\_W} = 0.14Z_{\text{lin}}{}^{0.47} . \quad (11)$$

As shown in Figure 4 (c_2, d_2), the fit for rain agrees rather well with that derived from field campaign observations [Matrosov, 2005; Matrosov, 2007].

Using these fits, we calculated the ratio of the specific attenuation of melting layer and rain, and found that it decreases from 4.3 to 1.5 and from 2.4 to 1.2 for Ka- and W-bands, respectively, as the reflectivity rises from 23 to 36 dBZ. A similar decreasing behavior of specific attenuation ratio was observed for X-band by Bellon et al. [1997] (see the comparison in supporting material).

5 Conclusions

In this paper, we present a technique for deriving the melting layer attenuation at Ka-and W-bands using X-, Ka- and W-band vertically pointing radar Doppler spectra. The retrieval is based on the measurements of differential attenuation, which avoids potential radar calibration and wet radome issues. Using data collected during US DOE ARM funded BAECC experiment, melting layer attenuation was derived and parametrized. The presented "sanity" check and case study show the necessity of utilizing the DSR_{ML_top} instead of simply using the reflectivity difference at the cloud top. Despite the limited observations (~ 48 min and ~24 min for Ka- and W-bands, respectively), the results show similar trends as previously found at X-band radar observations and agree reasonably well with the previously reported modeling studies. This agreement indicates a possibility of adopting simpler melting snowflake models for forward scattering computations. It is, however, found that the modeling-based attenuation parametrization seems to overestimate the attenuation for moderate to heavy rainfall. This difference could possibly be explained by the assumed snow microphysical properties that are used as input into the melting layer model. This stresses the need for more comprehensive modeling- and observation-based studies of melting layer properties.

Despite the focus of this study on deriving melting layer attenuation parametrizations, the proposed technique can be applied to mitigate the melting layer attenuation in ground-based radar measurements. This, however, requires multi-frequency radar observations with well-matched radar volumes. The application of this method to space- and aircraft- based observations is further complicated by the requirements of high-fidelity Doppler spectra measurements.

Mainly due to the expensive data storage in the past, spectra observations are still under-exploited. Long-term records of multi-frequency radar Doppler spectra are therefore expected to advance our knowledge on the melting layer, and to develop more realistic models for applications in commercial/satellite communications, ground/space borne radar remote sensing, quantitative precipitation estimation as well as radar data assimilation.

Acknowledgments

We would like to thank the personnel of Hyytiälä station and Matti Leskinen for their support in field observation. We further thank Stefan Kneifel from University of Cologne and Marta Tecla Falconi from University of Rome for helpful discussions. Three anonymous reviewers are also acknowledged for valuable suggestions and comments which helped to improve this article. The research of Haoran Li and Dmitri Moisseev was supported by Academy of Finland (Grant no. 305175) and the Academy of Finland Finnish Center of Excellence program (Grant no. 307331). Haoran Li was also funded by China Scholarship Council. The instrumentation used in this study was supported by NASA Global Precipitation Measurement Mission ground validation program and by the Office of Science U.S. Department of Energy ARM program. The BAECC data used in this study can be downloaded at http://www.archive.arm.gov/discovery/.

References

Andrić, J., Kumjian, M. R., Zrnić, D. S., Straka, J. M., & Melnikov, V. M. (2013). Polarimetric signatures above the melting layer in winter storms: An observational and modeling study. Journal of Applied Meteorology and Climatology, 52(3), 682-700

Battaglia, A., Kummerow, C., Shin, D. B., & Williams, C. (2003). Constraining microwave brightness temperatures by radar brightband observations. Journal of Atmospheric and Oceanic Technology, 20(6), 856-871

Bauer, P., Baptista, J. P., & De Iulis, M. (1999). The effect of the melting layer on the microwave emission of clouds over the ocean. Journal of the atmospheric sciences, 56(6), 852-867

Bellon, A., Zawadzki, I., & Fabry, F. (1997). Measurements of melting layer attenuation at X‐band frequencies. Radio Science, 32(3), 943-955

Botta, G., Aydin, K., & Verlinde, J. (2010). Modeling of microwave scattering from cloud ice crystal aggregates and melting aggregates: A new approach. IEEE Geoscience and Remote Sensing Letters, 7(3), 572-576

D'Amico, M. M., Holt, A. R., & Capsoni, C. (1998). An anisotropic model of the melting layer. Radio Science, 33(3), 535-552

Doviak, R. J., & Zrnic, D. S. (1984). Doppler Radar and WeatherObservations, Academic Press, New York.

Ellis, S. M., & Vivekanandan, J. (2011). Liquid water content estimates using simultaneous S and Ka band radar measurements. Radio Science, 46, RS2021, doi:10.1029/2010RS004361

Gaussiat, N., Sauvageot, H., & Illingworth, A. J. (2003). Cloud liquid water and ice content retrieval by multiwavelength radar. Journal of Atmospheric and Oceanic Technology, 20(9), 1264-1275

Fabry, F., & Zawadzki, I. (1995). Long-term radar observations of the melting layer of precipitation and their interpretation. Journal of the atmospheric sciences, 52(7), 838-851

Fabry, F., & Szyrmer, W. (1999). Modeling of the melting layer. Part II: Electromagnetic. Journal of the atmospheric sciences, 56(20), 3593-3600

Falconi, M. T., Lerber, A. V., Ori, D., Marzano, F. S., & Moisseev, D. (2018). Snowfall retrieval at X, Ka and W bands: consistency of backscattering and microphysical properties using BAECC ground-based measurements. Atmospheric Measurement Techniques, 11(5), 3059-3079

Haynes, J. M., L'Ecuyer, T. S., Stephens, G. L., Miller, S. D., Mitrescu, C., Wood, N. B., & Tanelli, S. (2009). Rainfall retrieval over the ocean with spaceborne W‐band radar. Journal of Geophysical Research: Atmospheres, 114(D8), doi:10.1029/2008JD009973

Hogan, R. J., Gaussiat, N., & Illingworth, A. J. (2005). Stratocumulus liquid water content from dual-wavelength radar. Journal of Atmospheric and Oceanic Technology, 22(8), 1207-1218

Hogan, R. J., Honeyager, R., Tyynelä, J., & Kneifel, S. (2017). Calculating the millimetre‐wave scattering phase function of snowflakes using the self‐similar Rayleigh–Gans

Approximation. Quarterly Journal of the Royal Meteorological Society, 143(703), 834-844

Hogan, R. J., Illingworth, A. J., & Sauvageot, H. (2000). Measuring crystal size in cirrus using 35- and 94-GHz radars. Journal of Atmospheric and Oceanic Technology, 17(1), 27-37

Hogan, R. J., & Westbrook, C. D. (2014). Equation for the microwave backscatter cross section of aggregate snowflakes using the self-similar Rayleigh–Gans approximation. Journal of the Atmospheric Sciences, 71(9), 3292-3301

Illingworth, A. J., Hogan, R. J., O'connor, E. J., Bouniol, D., Brooks, M. E., Delanoë, J., ... & Haeffelin, M. (2007). Cloudnet: Continuous evaluation of cloud profiles in seven operational models using ground-based observations. Bulletin of the American Meteorological Society, 88(6), 883-898

Johnson, B. T., Olson, W. S., & Skofronick-Jackson, G. (2016). The microwave properties of simulated melting precipitation particles: sensitivity to initial melting. Atmospheric Measurement Techniques, 9, 9-21, https://doi.org/10.5194/amt-9-9-2016

Kneifel, S., Kollias, P., Battaglia, A., Leinonen, J., Maahn, M., Kalesse, H., & Tridon, F. (2016). First observations of triple ‐ frequency radar Doppler spectra in snowfall: Interpretation and applications. Geophysical Research Letters, 43(5), 2225-2233. https://doi.org/10.1002/2015GL067618

Kneifel, S., Lerber, A., Tiira, J., Moisseev, D., Kollias, P., & Leinonen, J. (2015). Observed relations between snowfall microphysics and triple ‐ frequency radar measurements. Journal of Geophysical Research: Atmospheres, 120(12), 6034-6055

Kollias, P., B.A. Albrecht, & F. Marks. (2002). Why Mie?. Bull. Amer. Meteor. Soc., 83, 1471–1484, https://doi.org/10.1175/BAMS-83-10-1471

Kollias, P., & Albrecht, B. (2005). Why the melting layer radar reflectivity is not bright at 94 GHz. Geophysical research letters, 32, L24818. https://doi.org/10.1029/2005GL024074

Kollias, P., Rémillard, J., Luke, E., & Szyrmer, W. (2011). Cloud radar Doppler spectra in drizzling stratiform clouds: 1. Forward modeling and remote sensing applications. Journal of Geophysical Research: Atmospheres, 116(D13). https:// doi:10.1029/2010JD015237

Kollias, P., Jo, I., Borque, P., Tatarevic, A., Lamer, K., Bharadwaj, N., et al. (2014). Scanning ARM cloud radars. Part II: Data quality control and processing. Journal of Atmospheric and Oceanic Technology, 31(3), 583-598

Leinonen, J., D. N. Moisseev, V. Chandrasekar and J. Koskinen, (2011). Mapping Radar Reflectivity Values of Snowfall Between Frequency Bands. IEEE Trans. Geosci. Remote Sens., 49, (8), 3047 - 3058.

Leinonen, J. (2014). High-level interface to T-matrix scattering calculations: architecture, capabilities and limitations. Optics express, 22(2), 1655-1660

Leinonen, J., Kneifel, S., & Hogan, R. J. (2018). Evaluation of the Rayleigh–Gans approximation for microwave scattering by rimed snowflakes. Quarterly Journal of the Royal Meteorological Society, 144, 77-88

Leinonen, J., & von Lerber, A. (2018). Snowflake melting simulation using smoothed particle hydrodynamics. Journal of Geophysical Research: Atmospheres, 123, 1811–1825. https://doi.org/10.1002/2017JD027909

Li, H., Moisseev, D., & von Lerber, A. (2018). How does riming affect dual-polarization radar observations and snowflake shape? Journal of Geophysical Research: Atmospheres, 123. https://doi.org/10.1029/2017JD028186

Liao, L., Meneghini, R., Tian, L., & Heymsfield, G. M. (2009). Measurements and simulations of nadir-viewing radar returns from the melting layer at X and W bands. Journal of Applied Meteorology and Climatology, 48(11), 2215-2226.

Liebe, H. J. (1985). An updated model for millimeter wave propagation in moist air. Radio Science, 20(5), 1069-1089. http://dx.doi.org/10.1029/RS020i005p01069

Luke, E. P., Kollias, P., & Shupe, M. D. (2010). Detection of supercooled liquid in mixed‐phase clouds using radar Doppler spectra. Journal of Geophysical Research: Atmospheres, 115(D19), doi:10.1029/2009JD012884

Marshall, J. S., & Palmer, W. M. K. (1948). The distribution of raindrops with size. Journal of meteorology, 5(4), 165-166

Marshall, J. S., Hitschfeld, W., & Gunn, K. L. S. (1955). Advances in radar weather. Advances in geophysics, 2, 1-56

Matrosov, S. Y. (2005). Attenuation-based estimates of rainfall rates aloft with vertically pointing Ka-band radars. Journal of Atmospheric and Oceanic Technology, 22(1), 43-54

Matrosov, S. Y. (2007). Potential for attenuation‐based estimations of rainfall rate from CloudSat. Geophysical research letters, 34(5)

Matrosov, S. Y. (2008). Assessment of radar signal attenuation caused by the melting hydrometeor layer. IEEE Transactions on Geoscience and Remote Sensing, 46(4), 1039-1047

Matrosov, S. Y., Clark, K. A., & Kingsmill, D. E. (2007). A polarimetric radar approach to identify rain, melting-layer, and snow regions for applying corrections to vertical profiles of reflectivity. Journal of applied meteorology and climatology, 46(2), 154-166

Matsuo, T., & Sasyo, Y. (1981). Melting of snowflakes below freezing level in the atmosphere. Journal of the Meteorological Society of Japan. Ser. II, 59(1), 10-25

Mishchenko, M. I., & Travis, L. D. (1994). T-matrix computations of light scattering by large spheroidal particles. Optics communications, 109(1-2), 16-21

Mitrescu, C., L'Ecuyer, T., Haynes, J., Miller, S., & Turk, J. (2010). CloudSat precipitation profiling algorithm—Model description. Journal of Applied Meteorology and Climatology, 49(5), 991-1003

Moisseev, D. N., Chandrasekar, V., Unal, C. M. H., & Russchenberg, H. W. J. (2006). Dual-polarization spectral analysis for retrieval of effective raindrop shapes. Journal of atmospheric and oceanic technology, 23(12), 1682-1695

Nakamura, K., Kaneko, Y., Nakagawa, K., Hanado, H., & Nishikawa, M. (2018). Measurement Method for Specific Attenuation in the Melting Layer Using a Dual Ka-Band Radar System. IEEE Transactions on Geoscience and Remote Sensing, 56(6), 3511-3519

Olson, W. S., Bauer, P., Viltard, N. F., Johnson, D. E., Tao, W. K., Meneghini, R., & Liao, L. (2001). A melting-layer model for passive/active microwave remote sensing applications.

Part I: Model formulation and comparison with observations. Journal of Applied Meteorology, 40(7), 1145-1163

Panagopoulos, A. D., Arapoglou, P. D. M., & Cottis, P. G. (2004). Satellite communications at Ku, Ka, and V bands: Propagation impairments and mitigation techniques. IEEE Communications Surveys & Tutorials, 6(3), 2–14

Petäjä, T., O'Connor, E. J., Moisseev, D., Sinclair, V. A., Manninen, A. J., Väänänen, R., et al. (2016). BAECC: A field campaign to elucidate the impact of biogenic aerosols on clouds and climate. Bulletin of the American Meteorological Society, 97(10), 1909–1928. https://doi.org/10.1175/BAMS-D-14-00199.1

Planche, C., Wobrock, W., & Flossmann, A. I. (2014). The continuous melting process in a cloud‐scale model using a bin microphysics scheme. Quarterly Journal of the Royal Meteorological Society, 140(683), 1986-1996

Russchenberg, H. W. J., & Ligthart, L. P. (1996). Backscattering by and propagation through the melting layer of precipitation: A new polarimetric model. IEEE transactions on geoscience and remote sensing, 34(1), 3-14

Ryzhkov, A. V., & Zrnic, D. S. (1998). Discrimination between rain and snow with a polarimetric radar. Journal of Applied Meteorology, 37(10), 1228-1240

Schuur, T. J., Ryzhkov, A. V., Zrnić, D. S., & Schönhuber, M. (2001). Drop size distributions measured by a 2D video disdrometer: Comparison with dual-polarization radar data. Journal of Applied Meteorology, 40(6), 1019-1034

Sekelsky, S. M. (2002). Near-field reflectivity and antenna boresight gain corrections for millimeter-wave atmospheric radars. Journal of Atmospheric and Oceanic Technology, 19(4), 468-477

Shupe, M. D., Kollias, P., Matrosov, S. Y., & Schneider, T. L. (2004). Deriving mixed-phase cloud properties from Doppler radar spectra. Journal of Atmospheric and Oceanic Technology, 21(4), 660-670

Siles, G. A., Riera, J. M., & Garcia-del-Pino, P. (2015). Atmospheric attenuation in wireless communication systems at millimeter and THz frequencies [Wireless Corner]. IEEE Antennas and Propagation Magazine, 57(1), 48-61

Skaropoulos, N. C., & Russchenberg, H. W. (2003). Simulations of Doppler spectra in the melting layer of precipitation. Geophysical research letters, 30(12), 1634, doi:10.1029/2003GL016959

Spek, A.L., C.M. Unal, D.N. Moisseev, H.W. Russchenberg, V. Chandrasekar, & Y. Dufournet. (2008). A New Technique to Categorize and Retrieve the Microphysical Properties of Ice Particles above the Melting Layer Using Radar Dual-Polarization Spectral Analysis. J. Atmos. Oceanic Technol., 25, 482–497, https://doi.org/10.1175/2007JTECHA944.1

Stein, T. H., Westbrook, C. D., & Nicol, J. C. (2015). Fractal geometry of aggregate snowflakes revealed by triple‐wavelength radar measurements. Geophysical Research Letters, 42(1), 176-183.

Tuttle, J. D., & Rinehart, R. E. (1983). Attenuation correction in dual-wavelength analyses. Journal of climate and applied meteorology, 22(11), 1914-1921

Tridon, F., Battaglia, A., & Kollias, P. (2013). Disentangling Mie and attenuation effects in rain using a Ka ‐ W dual ‐ wavelength Doppler spectral ratio technique. Geophysical Research Letters, 40(20), 5548-5552, doi:10.1002/2013GL057454

Tridon, F., & Battaglia, A. (2015). Dual ‐ frequency radar Doppler spectral retrieval of rain drop size distributions and entangled dynamics variables. Journal of Geophysical Research: Atmospheres, 120(11), 5585-5601

Tridon, F., Battaglia, A., Luke, E., & Kollias, P. (2017a). Rain retrieval from dual ‐ frequency radar Doppler spectra: validation and potential for a midlatitude precipitating case ‐ study. Quarterly Journal of the Royal Meteorological Society, 143(704), 1364-1380

Tridon, F., Battaglia, A., & Watters, D. (2017b). Evaporation in action sensed by multiwavelength Doppler radars. Journal of Geophysical Research: Atmospheres, 122(17), 9379-9390

Tyynelä, J., Leinonen, J., Westbrook, C. D., Moisseev, D., & Nousiainen, T. (2013). Applicability of the Rayleigh ‐ Gans approximation for scattering by snowflakes at microwave frequencies in vertical incidence. Journal of Geophysical Research: Atmospheres, 118(4), 1826-1839

von Lerber, A., Moisseev, D., Leinonen, J., Koistinen, J., & Hallikainen, M. T. (2015). Modeling radar attenuation by a low melting layer with optimized model parameters at C-band. IEEE Transactions on Geoscience and Remote Sensing, 53(2), 724-737

Wielaard, D. J., Mishchenko, M. I., Macke, A., & Carlson, B. E. (1997). Improved T-matrix computations for large, nonabsorbing and weakly absorbing nonspherical particles and comparison with geometrical-optics approximation. Applied optics, 36(18), 4305-4313

Wolfensberger, D., Scipion, D., & Berne, A. (2016). Detection and characterization of the melting layer based on polarimetric radar scans. Quarterly Journal of the Royal Meteorological Society, 142, 108-124

Yokoyama, T., & Tanaka, H. (1984). Microphysical processes of melting snowflakes detected by two-wavelength radar. Part I. Principle of measurement based on model calculation. Journal of the Meteorological Society of Japan, 62(4), 650-666

Zawadzki, I., Fabry, F., & Szyrmer, W. (2001). Observations of supercooled water and secondary ice generation by a vertically pointing X-band Doppler radar. Atmospheric Research, 59, 343-359.

Zawadzki, I., Szyrmer, W., Bell, C., & Fabry, F. (2005). Modeling of the melting layer. Part III: The density effect. Journal of the atmospheric sciences, 62(10), 3705-3723

Zhang, W., Karhu, S. I., & Salonen, E. T. (1994). Predictions of radiowave attenuations due to a melting layer of precipitation. IEEE transactions on antennas and propagation, 42(4), 492-500

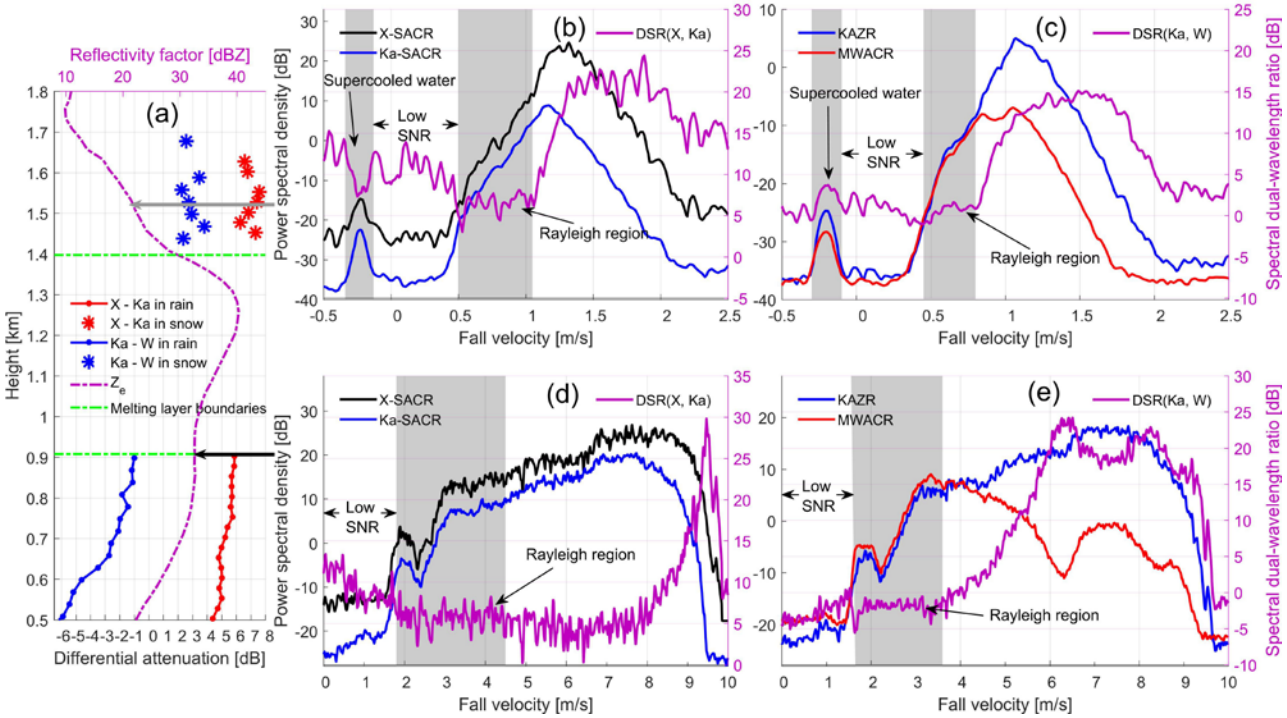

Figure 1. Differential attenuation and X-band observed reflectivity factor (a). Spectra observations in snow and rain areas indicated by the grey and black arrows are shown in panels (b, c) and (d, e) respectively. The grey shading identifies regions of spectra where hydrometeors are Rayleigh scatterers.

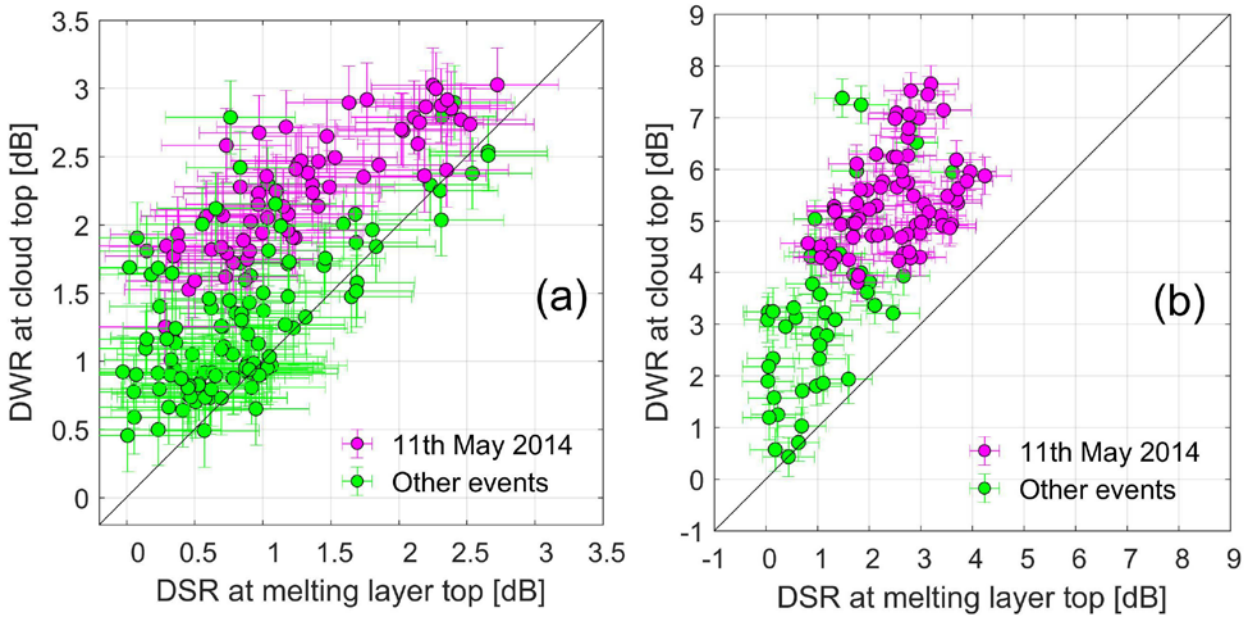

Figure 2. Comparison of calculated diffrential attenuations using DWR at cloud top and DSR at the melting layer top for X-SACR/Ka-SACR (a) and KAZR/MWACR (b). Note that dielectric factor for supercooled water in (b) was scaled to ice.

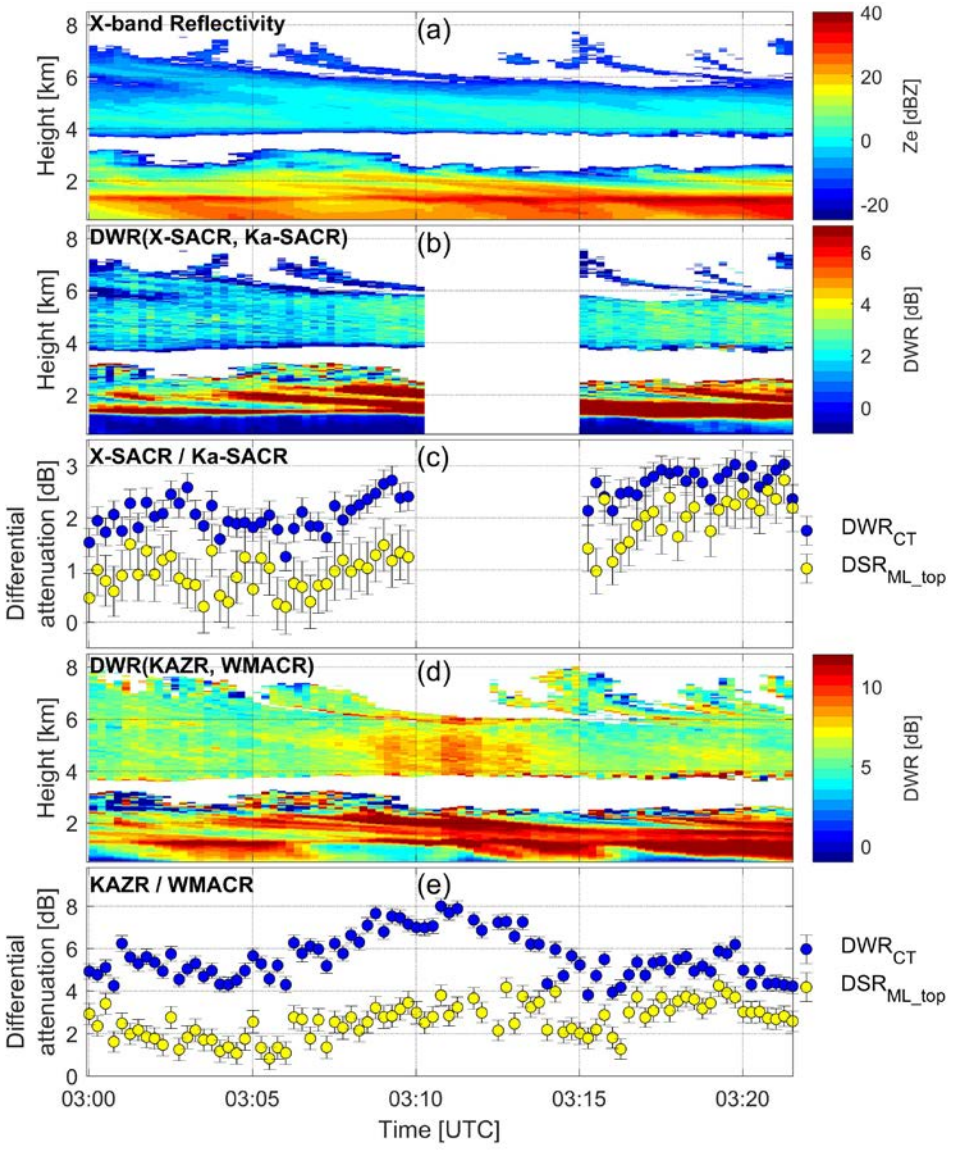

Figure 3. Differential attenuation in the melting layer for May 11th 2014 precipitation event. Radar reflectivity profiles observed by X-SACR are given in panel (a), DWR profiles for X-/Ka-SACR in (b) and KAZR/WMACR in (d). The retrieved melting layer differential attenuation from X-/Ka-SACR observations is shown in panel (c) and KAZR/WMACR in (e). Similar to Figure 2, panels (c) and (e) compare the DWR values calculated at cloud top and DSR values derived from the Rayleigh parts of spectra observations at melting layer top, respectively. The gaps during 03:10 ~ 03:15 in (b) and (c) are due to missing of X- and Ka-SACR spectra data.

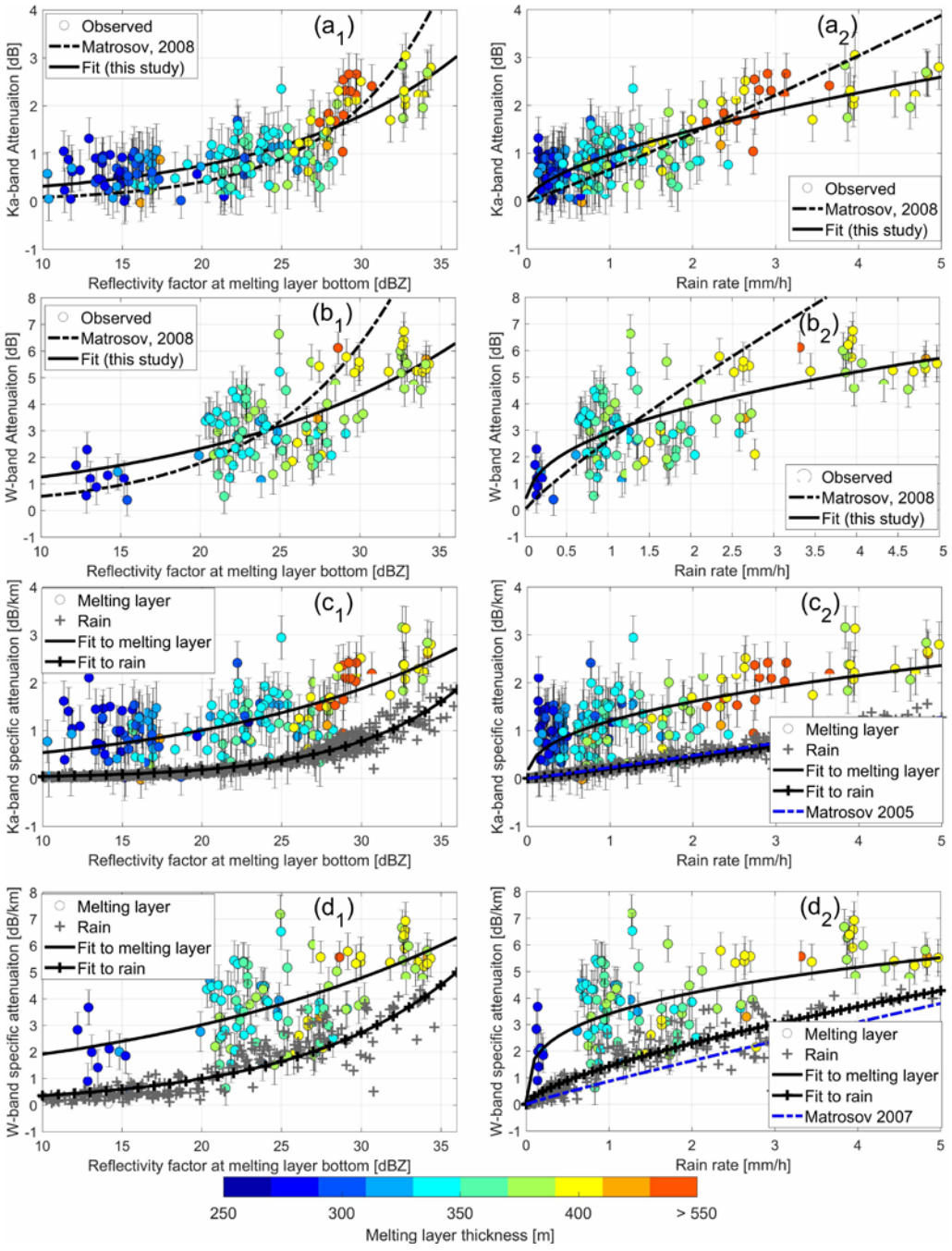

Figure 4. The derived melting-layer attenuation and specific attenuation for Ka-band (a and c) and W-band (b and d). The subscripts 1 and 2 indicate the functions of radar reflectivity factor and rain rate, respectively.